PHYSICAL REVIEW B **96**, 035422 (2017)

Anisotropic plasmons, excitons, and electron energy loss spectroscopy of phosphorene

Barun Ghosh,[1] Piyush Kumar,[2] Anmol Thakur,[1] Yogesh Singh Chauhan,[2] Somnath Bhowmick,[3] and Amit Agarwal[1,*]
[1]*Department of Physics, Indian Institute of Technology Kanpur, Kanpur 208016, India*
[2]*Department of Electrical Engineering, Indian Institute of Technology Kanpur, Kanpur 208016, India*
[3]*Department of Materials Science and Engineering, Indian Institute of Technology Kanpur, Kanpur 208016, India*

(Received 25 March 2017; published 18 July 2017)

In this article, we explore the anisotropic electron energy loss spectrum (EELS) in monolayer phosphorene based on *ab initio* time-dependent density-functional-theory calculations. Similarly to black phosphorus, the EELS of undoped monolayer phosphorene is characterized by anisotropic excitonic peaks for energies in the vicinity of the band gap and by interband plasmon peaks for higher energies. On doping, an additional intraband plasmon peak also appears for energies within the band gap. Similarly to other two-dimensional systems, the intraband plasmon peak disperses as $\omega_{\rm pl} \propto \sqrt{q}$ in both the zigzag and armchair directions in the long-wavelength limit and deviates for larger wave vectors. The anisotropy of the long-wavelength plasmon intraband dispersion is found to be inversely proportional to the square root of the ratio of the effective masses: $\omega_{\rm pl}(q\hat{y})/\omega_{\rm pl}(q\hat{x}) = \sqrt{m_x/m_y}$.

DOI: 10.1103/PhysRevB.96.035422

I. INTRODUCTION

Within the family of two-dimensional (2D) materials [1–12], phosphorene (few layers of black phosphorus)—a direct band-gap semiconductor with a puckered atomic structure—has a highly anisotropic band structure [6,7,13]. It has a massive Dirac-like energy dispersion along the armchair and a parabolic Schrödinger-like energy dispersion along the zigzag direction [14–17]. This results in highly anisotropic single-particle electronic [14], thermal [18], many-particle excitonic [19], and plasmonic properties [20]. The plasmon dispersion has been recently calculated based on low-energy continuum Hamiltonian, and it is found to be highly anisotropic [20,21] with different doping dependence in different directions, depending on the number of layers.

From an experimental viewpoint, momentum-resolved electron energy loss spectroscopy [22] (EELS) directly probes the loss function of a material, which in turn is simply the inverse of the imaginary part of the dynamical interacting dielectric constant of a material: $\mathcal{E}_{\rm Loss}(\mathbf{q},\omega) = -{\rm Im}[1/\epsilon_M(\mathbf{q},\omega)]$. It has been used extensively in a variety of materials, such as graphene [23–30], transition metal dichalcogenides [31,32], and bulk black phosphorus [33], to explore the single-particle and collective excitations such as excitons and plasmons. In terms of computational methods, calculations based on effective low-energy continuum [34,35] as well as the tight-binding Hamiltonian [36–38] are very insightful, but they fail to capture many of the experimental aspects of the EELS spectrum accurately; in particular the low-energy intraband plasmons at large wave vectors and the high-energy interband plasmons involving transitions across various energy bands. For example, in doped graphene, the low-energy [34,39,40] and tight-binding approach [36] fail to capture the plasmon anisotropy at finite wave vectors in the Γ-K and the Γ-M directions, which has been observed experimentally [26,27]. However, the loss function and corresponding plasmon dispersion relation is generally well described by density-functional-theory-based *ab initio* calculations [30,32,41–46]. In the case of phosphorene, the low-energy intraband plasmon spectrum has been studied using the continuum approximation [20,21]. Further, the effects of strain [37] and disorder [38] on the plasmon spectrum have been incorporated using a tight-binding approach, but to the best of our knowledge, there is no *ab initio*–based study of the anisotropic plasmon dispersion (both low as well as high energy) and the high-energy EELS spectrum of monolayer phosphorene. Motivated by this, we present an *ab initio* density-functional-theory- (DFT) based study of the anisotropic EELS spectrum, which includes low-energy intraband plasmons at finite doping, excitons, and interband plasmons in monolayer phosphorene.

We find that the crystal anisotropy of bulk black phosphorus is preserved down to its single layer, leading to a highly anisotropic electronic band structure, which results in a direction-dependent EELS. In the case of finite doping, we find an intraband plasmon mode which lies well below the band gap of phosphorene. Interestingly, it has a $\sqrt{q}$ dispersion for small wave vector in each of the two principal directions (parallel to the armchair and the zigzag edge of monolayer phosphorene), which signifies the two-dimensional nature of the plasmon mode. We also find a highly dispersive mode in the EELS, which appears at slightly higher energy than the band gap of phosphorene; it is identified as the exciton peak. Interestingly, while the exciton peak appears in the armchair direction, it is completely absent along the zigzag edge. The other high-energy peaks correspond to different interband transitions, with a very distinct peak appearing for energies close to 5 eV. We also observe a general trend that with increasing momentum transfer, all the resonant features (excitations) of the EELS spectrum are blue shifted and they gradually lose their strength.

The paper is organized as follows: In Sec. II, we discuss the formulation for calculating the interacting density response function and the corresponding EELS spectrum, along with the computational details of our *ab initio* study to get the electronic band structure of phosphorene. Next, we describe the calculated EELS spectrum in Sec. III, followed by a detailed discussion focused on anisotropy of intraband plasmons in Sec. IV. Finally, we summarize our findings in Sec. V.

---

[*] amitag@iitk.com

II. THEORY AND COMPUTATIONAL DETAILS

A. Dynamical dielectric and loss function

Our starting point is the noninteracting density-density response function ($\chi^0_{\mathbf{G}\mathbf{G}'}$) for a periodic lattice, which is obtained from the Adler-Wiser formula given by [47,48]

$$\begin{aligned}\chi^0_{\mathbf{G}\mathbf{G}'}(\mathbf{q},\omega) = \frac{1}{\Omega}\sum_{\mathbf{k}}^{\mathrm{BZ}}\sum_{n,n'}\frac{f_{n\mathbf{k}} - f_{n'\mathbf{k}+\mathbf{q}}}{\omega + \epsilon_{n\mathbf{k}} - \epsilon_{n'\mathbf{k}+\mathbf{q}} + i\eta} \\ \times \langle\psi_{n\mathbf{k}}|e^{-i(\mathbf{q}+\mathbf{G})\cdot\mathbf{r}}|\psi_{n'\mathbf{k}+\mathbf{q}}\rangle_{\Omega_{\mathrm{cell}}} \\ \times \langle\psi_{n\mathbf{k}}|e^{i(\mathbf{q}+\mathbf{G}')\cdot\mathbf{r}'}|\psi_{n'\mathbf{k}+\mathbf{q}}\rangle_{\Omega_{\mathrm{cell}}}.\end{aligned} \tag{1}$$

The Kohn-Sham energy eigenvalues $\epsilon_{n\mathbf{k}}$, the wave function $\psi_{n\mathbf{k}}$, and the corresponding Fermi-Dirac occupation function $f_{n\mathbf{k}}$ for the nth band at wave vector $\mathbf{k}$ are obtained from the ground-state calculations performed using the density functional theory.

Within the framework of time-dependent density functional theory (TDDFT) the interacting density-density response function can be obtained by solving a Dyson-type equation. Expanding in a plane-wave basis (valid for a periodic system), the interacting response function can be expressed as

$$\begin{aligned}\chi_{\mathbf{G}\mathbf{G}'}(\mathbf{q},\omega) = \chi^0_{\mathbf{G}\mathbf{G}'}(\mathbf{q},\omega) \\ + \sum_{\mathbf{G}_1,\mathbf{G}_2}\chi^0_{\mathbf{G}\mathbf{G}_1}(\mathbf{q},\omega)K_{\mathbf{G}_1\mathbf{G}_2}(q)\chi_{\mathbf{G}\mathbf{G}_2}(\mathbf{q},\omega),\end{aligned} \tag{2}$$

where $\mathbf{G}$ and $\mathbf{q}$ are the reciprocal lattice vector and the wave vector, respectively, and $K_{\mathbf{G}_1\mathbf{G}_2}$ is the (2D truncated for monolayer phosphorene) Coulomb kernel as described in Ref. [49]. The exchange-correlation part of the kernel is neglected within the framework of the random phase approximation (RPA). Using the $\chi_{\mathbf{G}\mathbf{G}'}$ matrix, the *microscopic dielectric matrix* is defined as

$$\epsilon_{\mathbf{G}\mathbf{G}'}(\mathbf{q},\omega) = [\delta_{\mathbf{G}\mathbf{G}'} + K_{\mathbf{G}\mathbf{G}'}(q)\chi_{\mathbf{G}\mathbf{G}'}]^{-1}. \tag{3}$$

The *macroscopic dielectric function* (ϵ_M) is given by the first diagonal element of the microscopic dielectric matrix obtained after inverting the right-hand side of Eq. (3):

$$\epsilon_M(\mathbf{q},\omega) = [\epsilon_{\mathbf{G}\mathbf{G}'}(\mathbf{q},\omega)]_{\mathbf{G}=\mathbf{G}'=0}. \tag{4}$$

Note that in a homogeneous electron gas $1/\epsilon_{\mathbf{G}\mathbf{G}'}$ [right-hand side of Eq. (3)] is a diagonal matrix and we have $\epsilon_M = 1 + K_{00}(q)\chi_{00}$. This is akin to taking a macroscopic average over the unit cell response and neglecting local polarization effects within the unit cell [48]. However, in a crystal, which is inhomogeneous and polarizable on a microscopic scale, the of-diagonal elements in Eq. (3) also contribute to the $\mathbf{G} = \mathbf{0},\mathbf{G}' = \mathbf{0}$ element of $\epsilon_{\mathbf{G}\mathbf{G}'}$, thus including the so-called local field effects.

The dynamical loss function, which is directly related to the EELS, is calculated as

$$\mathcal{E}_{\mathrm{Loss}}(\mathbf{q},\omega) = -\mathrm{Im}\big[\epsilon_M^{-1}(q,\omega)\big]. \tag{5}$$

Plasmons (collective density excitations) are characterized by the zeros of the real part of the macroscopic dielectric function (the denominator of the density-density response function within RPA).

B. Computational details

Electronic band-structure calculations are performed using density functional theory, as implemented in the GPAW package [50–52]. The kinetic energy cutoff for the plane-wave basis set is taken to be 500 eV. Initially, all the atomic positions are relaxed (within GGA) until the forces on each atom are less than 0.001 eV/Å. Next, we calculate the single-particle states [to be used as input for evaluating the response function in Eq. (1)] using the Gritsenko–van Leeuwen–van Lenthe–Baerends—solid-correlation potential (GLLB-SC) which has been found to improve the band gap in case of semiconductors [53]. While a k-point grid of 16 × 22 × 6 (16 × 22 × 1) is used for the Brillouin zone integrations of the bulk (monolayer) structure, for the electronic band-structure calculation, a much denser k-point grid of 32 × 44 × 14 (64 × 88 × 1) is used for calculating the q dependence of the EELS, giving a momentum resolution of ~0.043 Å^{-1} and ~0.0215 Å^{-1}, respectively, for the bulk and the monolayer phosphorene. In the case of the latter, we use a vacuum layer of 20 Å in the direction perpendicular to the phosphorene plane to suppress any interaction between two replica images in the vertical direction.

EELS calculations are performed using the generalized RPA. The generalized RPA uses the local field factors to add the impact of the exchange and correlation effects to the Hartree field [54]. Because of its long-range nature, the Coulomb potential of one layer can interact with its periodic replicas, which is avoided by taking a 2D truncated Coulomb kernel, following Ref. [49]. We consider up to 50 empty bands to correctly describe all the electronic excitations. For the local field corrections, a cut-off energy of 50 eV is used for

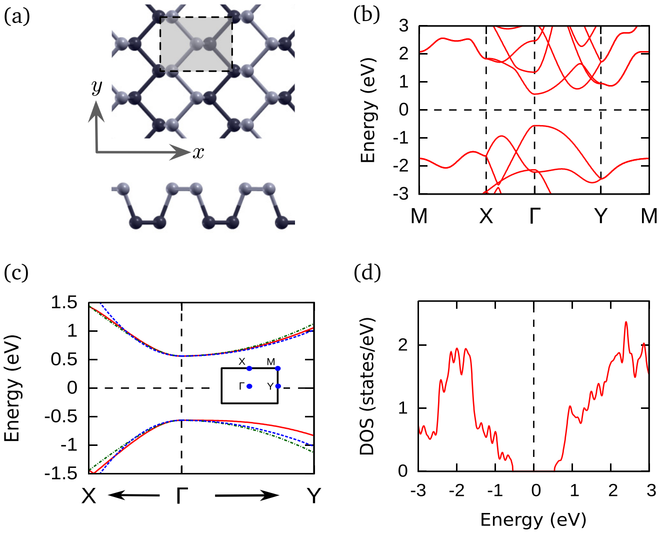

FIG. 1. (a) Geometric structure of phosphorene monolayer: top and side views with the shaded region indicating the unit cell. (b) The electronic band structure of phosphorene monolayer along the high symmetry axes, calculated using the GLLB-SC functional. (c) The comparison of the effective low-energy Hamiltonian in Eq. (6) (green dashed line) and Eq. (8) (blue dashed line), with the DFT band structure (red line) in the vicinity of the Γ point. (d) The corresponding density of states.

the **G** and **G**′ vectors, which corresponds to 259 (135) plane waves for monolayer phosphorene (bulk black phosphorus). The broadening parameter in Eq. (3) is taken to be $\eta = 0.05$ eV. Doping or the change in carrier concentration is achieved by shifting the position of the Fermi energy (E_f).

C. Electronic band structure of phosphorene

Phosphorene has a layered structure with each phosphorus atom covalently bonded with three adjacent atoms, forming a sp^3 hybridized puckered honeycomb structure [see Fig. 1(a)]. As shown in the figure, mutually perpendicular armchair and zigzag directions are aligned along the x and y axes, respectively. The lattice parameters of the bulk unit cell are found to be $a = 4.56$ Å (armchair), $b = 3.31$ Å (zigzag), and $c = 11.30$ Å, which are in good agreement with the values reported in the literature [6]. As shown in Fig. 1(a), Γ-X and Γ-Y are the high symmetry directions in the reciprocal lattice, which are aligned along the armchair and zigzag axes, respectively. Based on previous reports of large anisotropy of calculated and measured electronic and optical properties along these particular directions, in this paper we calculate and compare the EELS spectrum and the intraband low-energy plasmon dispersion along Γ-X and Γ-Y, respectively.

As reported in the literature, monolayer phosphorene is found to be a direct band-gap semiconductor, the magnitude of the gap being 1.51 eV (0.91 eV), calculated using the HSE06 (GGA-PBE) functional [14,55,56]. The GLLB-SC-computed electronic band structure has a direct band gap of 1.13 eV and it is shown in Fig. 1, along with the corresponding density of states (DOS). The conduction band minima (CBM) and the valance band maxima (VBM) are located at the Γ point. Interestingly, the electron dispersion is anisotropic and "semi-Dirac"-like around this point [see Fig. 1(b)], having a massive Dirac character along the Γ-X direction and parabolic with a large effective mass along the Γ-Y direction [57]. This highly anisotropic low-energy dispersion of phosphorene is the origin of the direction-dependent transport and optical properties of phosphorene.

Pristine phosphorene, being a relatively large band-gap semiconductor, has vanishingly small thermally excited charge carriers even at room temperature and, consequently, intraband plasmons are absent. In order to explore intraband plasmons, we consider phosphorene doped via electrostatic doping (controlled by a varying gate voltage). For electrostatic doping, the bands near the CBM (and thus the DOS) remain unaffected but the Fermi energy shifts to the conduction band, giving rise to doped (electronic) charge carriers, whose number density can be tuned by controlling the gate voltage.

The effective low-energy Hamiltonian and band structure of monolayer phosphorene has been derived using the $\mathbf{k}\cdot\mathbf{p}$ method [15] as well as the tight-binding approach [16,17,60,61], both of which yield a qualitatively similar picture [57]. For this manuscript, we work with the bare minimum effective low-energy Hamiltonian of phosphorene, retaining only the lowest-order terms in the wave vectors [62],

$$H = \left(uk_y^2 + \Delta\right)\sigma_x + v_f k_x \sigma_y, \tag{6}$$

where σ_i's are the Pauli matrices. The anisotropic energy spectrum is thus given by

$$E_s(\mathbf{k}) = s\sqrt{v_f^2 k_x^2 + \left(uk_y^2 + \Delta\right)^2}, \tag{7}$$

where $s = +1$ ($s = -1$) corresponds to the conduction (valance) band. Fitting Eq. (7) to our GLLB-SC dispersion in the vicinity of the Γ point [see Fig. 1(c)] yields $\Delta = 0.56$ eV, $u = 3.55$ eV Å^2, and $v_f = 4.75$ eV Å. Note that Eq. (7) can further be approximated as an anisotropic parabolic dispersion

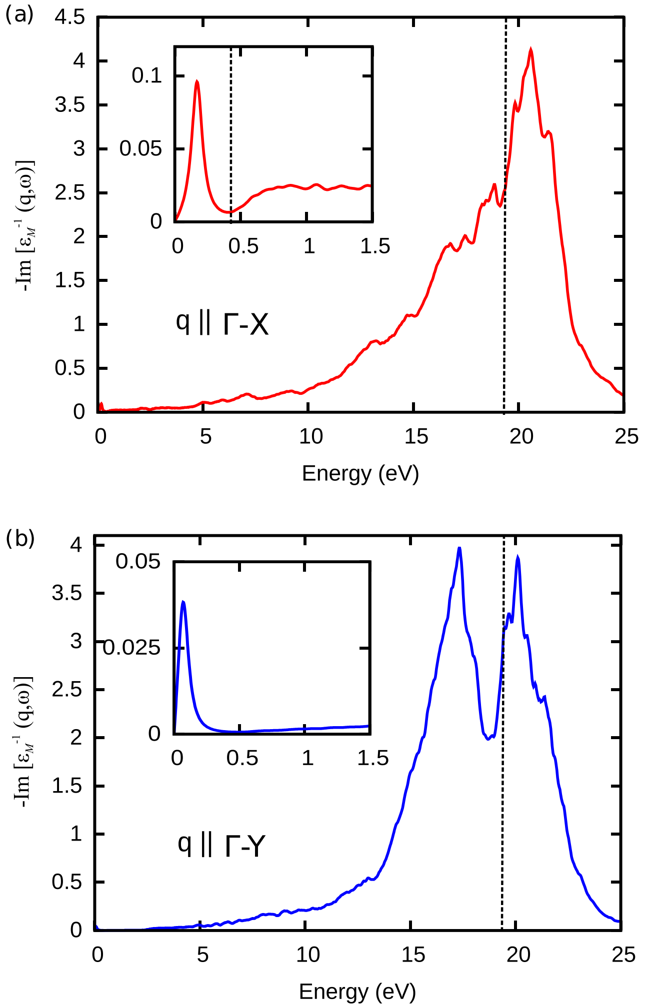

FIG. 2. $\mathcal{E}_{\text{Loss}}(\mathbf{q},\omega) = -\text{Im}[\epsilon_M^{-1}(q,\omega)]$ (in arbitrary units) of doped bulk black phosphorus along (a) Γ-X (armchair) and (b) Γ-Y (zigzag) directions as a function of energy for $q = 0.043$ Å^{-1}. The corresponding insets show the low energy behavior. The low energy peaks for $E \sim 0.2$ eV correspond to the intraband plasmon modes of doped black phosphorus. Other high-energy peaks correspond to anisotropic excitons (0.35 eV $< E < 2$ eV) and interband plasmonic excitations ($E > 2$ eV), both of which are identical for the doped as well as the undoped material. The dashed vertical lines in panels (a) and (b) represent the experimentally observed interband plasmon peak at 19.3 eV in Ref. [58]. The dashed vertical line in the inset of (a) marks the experimentally observed exciton peak (at 0.44 eV) in Ref. [59]. We have chosen $E_f = 95$ meV (measured from the conduction band bottom) for both the panels.

given by

$$E_c(\mathbf{k}) = E_c + \frac{\hbar^2 k_x^2}{2m_x} + \frac{\hbar^2 k_y^2}{2m_y}, \tag{8}$$

where $E_c = \Delta$. The values of the anisotropic effective masses for the conduction band are given by $m_x \equiv \hbar^2\Delta/v_f^2 = 0.20m_e$ and $m_y \equiv \hbar^2/(2u) = 1.1m_e$, with m_e being the electrons rest mass, consistent with earlier studies [14]. Equations (6) and (7) will be used to obtain the low-energy and low-momentum transfer plasmon dispersion of monolayer phosphorene analytically for comparison with our *ab initio* results.

III. ELECTRON ENERGY LOSS SPECTRUM

Having discussed the *ab initio* and the low-energy electronic band structure, we now proceed to calculate the EELS spectrum of phosphorene. We first test the methodology by calculating the EELS spectrum of bulk black phosphorus and comparing the same with reported data [33,58]. The computed EELS spectrum of bulk black phosphorus is shown in Fig. 2. As expected, the anisotropic nature of the electronic band structure of bulk phosphorus is manifested in the EELS data. The high-energy interband plasmon peak, present in the vicinity of 20 eV in both the Γ-X and the Γ-Y direction, is in good agreement with the recently published experimental EELS results for bulk black phosphorus [58]. The low-energy part of the spectrum, representing intraband plasmons and excitons, are shown in the inset of Fig. 2, and a marked anisotropy along the two principal direction is observed. In particular, the low-energy exciton peak in black phosphorus [see the continuous spectrum for energies >0.4 eV in the inset of Fig. 2(a)] is only present in the Γ-X (armchair) direction, which is consistent with recently reported measurements [33]. Also, the intraband plasmons in the armchair direction (Γ-X) have a higher intensity as opposed to those in the zigzag (Γ-Y) direction.

After benchmarking the methodology by successfully reproducing the characteristic features of EELS of bulk black phosphorus, we now focus on monolayer phosphorene. Due to obvious reasons related to its electronic band structure [see Fig. 1(b)], the EELS of monolayer phosphorene is also found to be highly anisotropic. This can clearly be observed in Figs. 3(a) and 3(b), where the calculated spectrum of a single layer of doped (by taking $E_f = 50$ meV, measured from the CBM) phosphorene is plotted for momentum transfer (q) along the Γ-X (armchair) and Γ-Y (zigzag) directions, respectively. Note that while the lowest-energy peak due to the intraband plasmons are observed only in the case of finite doping, others appearing at higher energy have intrinsic origin related to excitons and interband plasmons and they are present in undoped phosphorene as well. Specific features of the EELS are discussed in detail in the following subsections.

A. Intraband plasmons

As shown in Fig. 3 and Fig. 4, the first peak appears for energies less than 0.25 eV. The energy corresponding to the peak is well below the band gap of the pristine monolayer phosphorene and, in addition, this peak is absent in case of undoped phosphorene. Thus we interpret this as the peak originating from the intraband plasmon modes. With increasing momentum transfer, the intensity of intraband plasmons decreases and the peak position shifts to a higher energy in both the Γ-X and Γ-Y directions (see Fig. 3 and Fig. 4). A similar type of blue shift is observed as the doping is increased. As with bulk black phsophorous, the intensity of the intraband peak is lower for momentum transfer along the Γ-Y direction compared to the Γ-X direction, which has the maximum intensity among all the EELS peaks at $q \to 0$ [see Fig. 3]. The anisotropy of intraband plasmon modes and their momentum and doping dependence are discussed in detail in Sec. IV. Note that the finite width of the intraband plasmon mode in Figs. 3 and 4 indicates the existence of some damping mechanism even for small q. This is a consequence of retaining a finite $\eta = 0.05$ eV in our calculations for the polarization function—see Eq. (1).

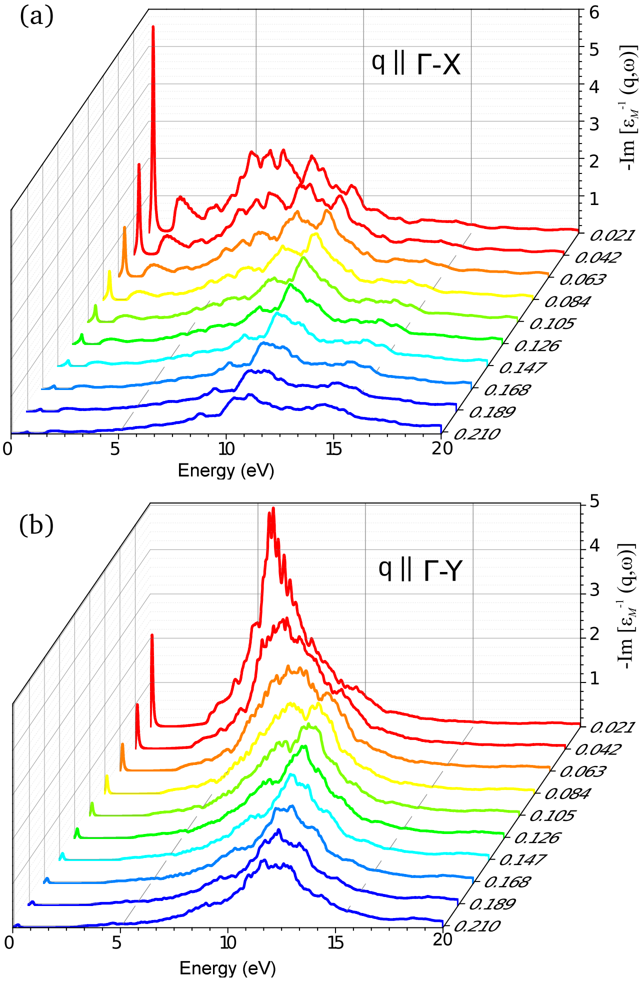

FIG. 3. EELS (in arbitrary units) of monolayer phosphorene along the (a) Γ-X (armchair) and (b) Γ-Y (zigzag) directions for different values of momentum transfer as a function of q and energy (measured from the bottom of the conduction band). The low-energy peaks ($E < 1$ eV) correspond to the intraband plasmons which appear only for the doped case. Other high-energy peaks and features corresponding to the excitons and interband plasmonic excitations are identical for the doped and undoped cases.

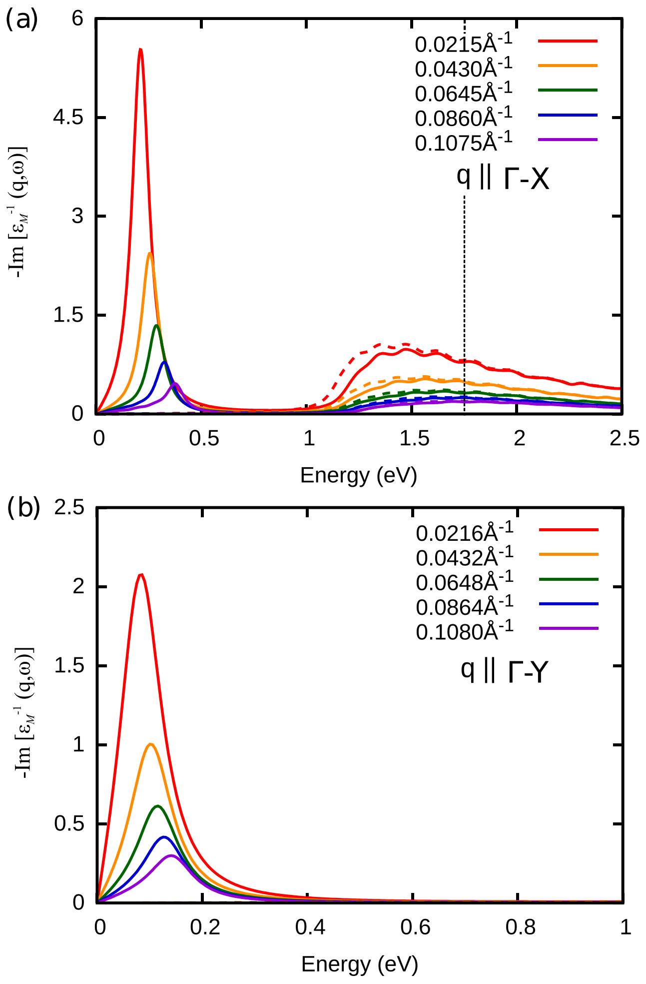

FIG. 4. Low-energy part of the EELS spectrum of monolayer phosphorene for momentum transfer along the (a) Γ-X and (b) Γ-Y directions. The solid lines denote the doped case with $E_f = 50$ meV, and the dashed line corresponds to the pristine undoped material. The dashed vertical line in panel (a) represents the experimentally observed exciton peak (at 1.73 eV) in Ref. [59]. The lowest-energy peak ($E < 1$ eV) arises from the intraband charge density excitation (plasmon) which is present only in the doped case. The slightly higher energy ($E \sim 1$ eV) peak which is present only for the momentum transfer along the Γ-X direction corresponds to the exciton (electron-hole bound pair). Both the modes are highly dispersive in nature and they gradually loose their strength with increasing momentum transfer. Note that, in panel (b), the dashed lines corresponding to the undoped case, are identically equal to zero due to the absence of the exciton peak.

B. Low-energy excitons

The next peak in the EELS is observed in the vicinity of 1.3 eV, which is gradually shifted towards the higher energy, accompanied by intensity reduction with increasing q. This peak is much more dispersive compared to the intraband plasmon peaks and extends approximately up to 3 eV (see Fig. 3 and Fig. 4). Since the peak energy coincides approximately with the energy gap of monolayer phosphorene and it exists in undoped phosphorene as well and it is almost independent of doping, we identify this as the lowest-energy excitonic peak. As shown in Fig. 3 and Fig. 4, the excitonic peak is highly anisotropic in nature, as it appears only in the case of momentum transfer along the Γ-X direction while being completely absent along the Γ-Y. We believe that the strongly anisotropic optical response reported for monolayer black phosphorene, which is transparent to the incident light in the energy range of 1.1–2.5 eV, but only if it is polarized along the zigzag direction and opaque if the light is polarized in the armchair direction [19,33], originates from the anisotropy of the lowest-energy electron-hole pair excitation observed in this work. Note that, since the crystal anisotropy observed in monolayer persists for multilayer, as well as bulk black phosphorus, a similar kind of anisotropic excitonic response is expected at higher thickness as well.

C. Interband high-energy plasmons

As we move towards higher energy, the next prominent EELS peak appears in the vicinity of 5 eV, and, similarly to the low energy peaks, its intensity reduces accompanied by a blue shift with increasing momentum transfer. Though it is also anisotropic in nature, this peak has a higher intensity along the zigzag direction as compared to the armchair direction—unlike the case of intraband plasmons. As expected, this high-energy peak is nearly independent of doping, as it corresponds to very high energy interband transitions.

Comparing the EELS intensity of various peaks as a function of q, it is clear that in general the EELS intensity is maximum for direct transitions with $q \to 0$ and decays with increasing q. However, the low-energy intraband plasmon peak decays more rapidly with increasing q (on account of damping by multiple electron-hole excitations) as compared to the high-energy peaks associated with interband transitions. For example, in case of $q \parallel \Gamma - X$, the intraband plasmon peak is the most intense among all the EELS peaks for ($q = 0.021$ Å^{-1}), which almost vanishes at higher q, leaving the interband transition peak around 10–14 eV to be the most prominent one. Due to its anisotropic nature, the scenario differs in the case of $q \parallel \Gamma - Y$, where the interband transition peak around 5 eV has the highest intensity (at $q = 0.021$ Å^{-1}) among all the EELS peaks and it broadens significantly and shifts to around 10–14 eV at higher value of q.

Note that, other than the intraband plasmons, the rest of the peaks corresponding to the interband transitions are likely to be affected due to the band-gap underestimation (approximately 40%) of GLLB-SC-based electronic band-structure calculations. For example, while the GW band gap is reported to be 1.84 eV [14,56] for monolayer black phosphorus, the GLLB-SC based band gap is found to be 1.13 eV in our calculation. Thus, the EELS peaks corresponding to interband transitions are expected to be blue shifted in an actual experiment. However, the GLLB-SC band-gap estimation of 0.35 eV for bulk black phosphorus is very close to its experimentally reported value of 0.31–0.35 eV [56]. Thus it turns out that for bulk black phosphorus, an EELS peak of ∼20 eV (as shown in Fig. 2) based on GLLB-SC calculations is consistent with the 19.3-eV peak observed in recent experiments [58]. The band gap, the exciton peak, and the corresponding interband plasmon energy have been probed in different works, and the

TABLE I. The energy scale of the various experimentally reported features for bulk and monolayer black phosphorus: the band gap (E_g), exciton peak (E_{exciton}), and the interband plasmon (E_{inter}) (for $q = 0$ case) based on photoluminance (PL), transmission electron microscopy (TEM), and scanning TEM (STEM) experiments.

Material	E_g (eV)	Method	E_{exciton} (eV)	E_{inter} (eV)	Ref.
Bulk	0.35	PL	0.35	–	[59]
Bulk	–	TEM	0.44	–	[33]
Bulk	–	STEM	–	19.3	[58]
Bulk	0.35	DFT	∼0.5	∼20.0	This work
1L	1.73	PL	1.73	–	[59]
1L	1.32	PL	1.32	–	[63]
1L	1.45	PL	1.45	–	[6]
1L	1.13	DFT	∼1.4	∼5.0	This work

experimental results are summarized in Table I, along with our GLLB-SC-based estimated values.

IV. ANISOTROPIC INTRABAND PLASMONS

Having described the prominent features of the EELS spectrum of monolayer phosphorene, we now focus on the anisotropic nature of the low-energy intraband plasmons and investigate their q and doping (E_f) dependence. The low-energy loss function along the Γ-X and Γ-Y directions is shown in Figs. 4(a) and 4(b), respectively. As discussed earlier, the first low-energy peak which appears for energies significantly below the band gap of phosphorene and only present in the case of finite doping corresponds to intraband plasmons or collective charge density excitations. As shown in Fig. 4, the intraband plasmon peak has higher intensity along the Γ-X direction as compared to the Γ-Y direction, similarly to the case of bulk phosphorus. Interestingly, the intensity decay and blue shift of the intraband plasmon peak is more rapid in the Γ-X direction compared to the Γ-Y direction.

The momentum dependence of the intraband plasmon peak is further analyzed at different doping (by varying the Fermi energy) in Fig. 5. As shown in the figure, for relatively small momentum transfers, the dispersion follows the universal long wavelength $\sqrt{q}$ behavior which is ubiquitous in two-dimensional systems [35]. For higher values of the momentum transfer q, a clear deviation from the $\sqrt{q}$ behavior is observed. As shown in Fig. 5, increasing the doping extends the range of validity of $\sqrt{q}$ behavior. For example, at $E_f = 50$ meV the $\sqrt{q}$ fit along the Γ-X direction holds up to $q = 0.1\,\text{Å}^{-1}$, which extends up to $q = 0.15\,\text{Å}^{-1}$ with increased doping ($E_f = 90$ meV). Similar behavior of the plasmon dispersion is also seen along the Γ-Y direction, albeit the spectral weight of the corresponding plasmon peak is smaller in the Γ-Y direction.

In a very clean system, the prominent damping channel for the plasmon mode is expected to be Landau damping: The plasmon mode decays into the single-particle continuum of the conduction band, whose boundary is marked by the maxima of $E_c^{\text{sp}}(\mathbf{q}) = E(\Gamma + \mathbf{q}) - E(\Gamma)$ for E_f close to the conduction band bottom—see the shaded area in Fig. 5. Outside this region the plasmon is (ideally) supposed to be completely undamped. However, in actual calculations the plasmon damping is introduced via the finite value of η [see Eq. (1)] in the calculation of the polarization function. This is a qualitative way of accounting for very small disorder in the system. Additionally, the plasmon damping also arises due to multi-particle excitations, which in our calculations are included via the local field corrections.

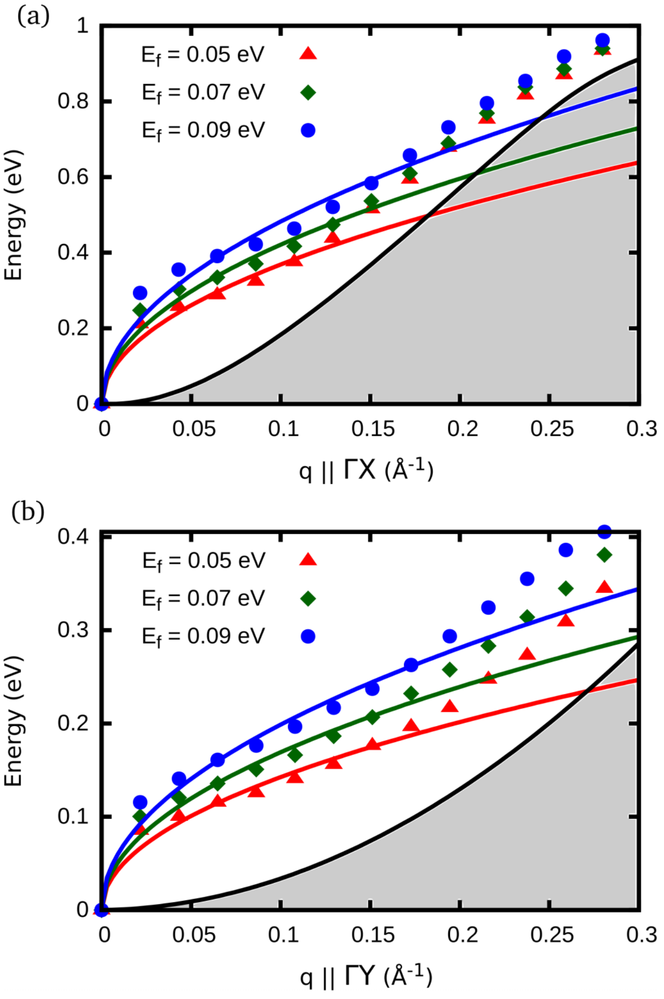

FIG. 5. Intraband plasmon dispersion of monolayer phosphorene along the (a) Γ-X and (b) Γ-Y directions at different doping. The corresponding solid lines denote the “universal” long-wavelength $\sqrt{q}$ dependence of the plasmon dispersion in two dimensions, which is valid for small q values only. The shaded region in both the panels denotes the single-particle continuum (electron-hole excitation spectrum) of the conduction band which is marked by the maxima of $E_c^{\text{sp}}(\mathbf{q}) = E_c(\Gamma + \mathbf{q}) - E_c(\Gamma)$ for $E_f (= 0.05$ eV) close to the conduction band bottom.

Starting from the anisotropic parabolic approximation of the band structure of monolayer phosphorene, given by Eq. (8), the low-energy plasmon dispersion within the RPA (for the Coulomb potential $V_q = 2\pi e^2/\epsilon q$) has been obtained in Ref. [21]. It is explicitly given by

$$\omega_{\text{pl}}(\mathbf{q}) = \alpha_0 (E_f - E_c)^{1/2} \left[\cos^2\theta_q + \frac{m_x}{m_y} \sin^2\theta_q \right]^{1/2} \sqrt{q}, \quad (9)$$

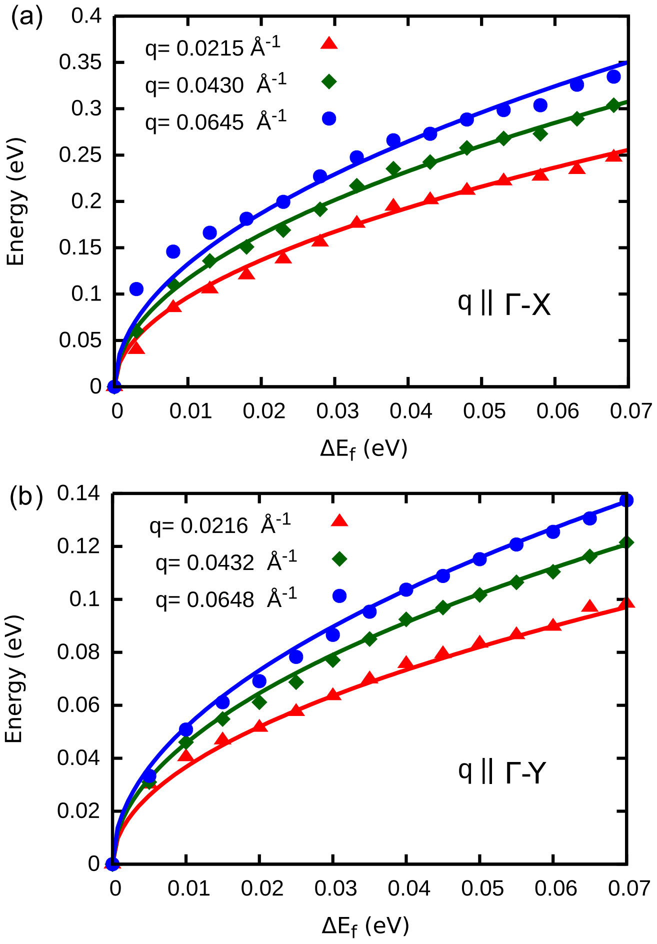

FIG. 6. Variation of the intraband plasmon energy with the electron doping specified by $\Delta E_f = E_f - E_c$ along the (a) Γ-X and (b) Γ-Y directions for different momentum transfer vectors. The doping dependence is of the plasmon dispersion for small q seems to be proportional to $\sqrt{E_f - E_c}$, consistent with Eq. (9).

where $\theta_q = \tan^{-1}(q_y/q_x)$, $\alpha_0^2 = 2\pi e^2 g_{2\rm d}/(m_x\epsilon)$, and $g_{2\rm d} = \sqrt{m_x m_y}/(\pi\hbar^2)$ is the two-dimensional density of states for an anisotropic parabolic band system. Equation (9) directly yields the following: (1) $\sqrt{q}$ dependence of the plasmon dispersion in all directions for small wave vectors, (2) $\sqrt{E_f - E_c}$ dependence of the low-energy (and low-wave-vector) plasmon dispersion on the Fermi energy, and (3) the long-wavelength anisotropy of the plasmon dispersion $\omega_{\rm pl}(q\hat{x})/\omega_{\rm pl}(q\hat{y}) = \sqrt{m_y/m_x}$, independent of the doping in the system.

The doping dependence of the intraband plasmon dispersion is shown in Fig. 6, and it clearly shows a reasonable match of the plasmon dispersion with the expected $\omega_{\rm pl} \propto \sqrt{E_f - E_c}$ dependence of the Fermi energy for small q. The plasmon frequency anisotropy ratio is shown in Fig. 7 and it also seems to be more or less consistent with the $\omega_{\rm pl}(q\hat{x})/\omega_{\rm pl}(q\hat{y}) = \sqrt{m_y/m_x}$ behavior. A more thorough calculation of the long-wavelength plasmon dispersion using the semi-Dirac continuum Hamiltonian for phosphorene [see Eq. (6)], is presented in the Appendix, and it also yields qualitatively similar results. However, the anisotropy ratio now explicitly depends on the Fermi energy—see Eq. (A10). However, we note that this E_f dependence of the anisotropic ratio of the plasmon frequency is small, as shown in Fig. 7(b).

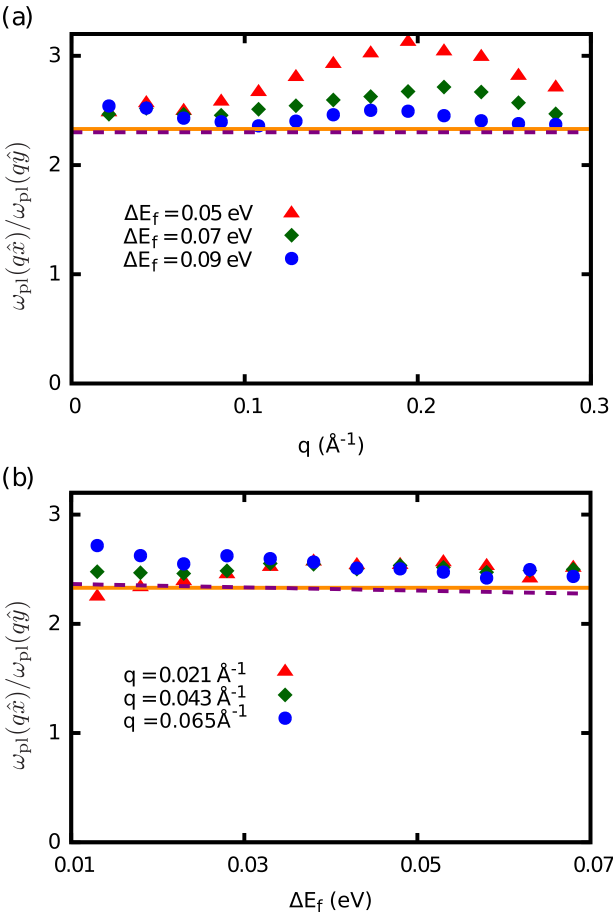

FIG. 7. Variation of the plasmon anisotropy ratio, $\omega_{\rm pl}(q\hat{x})/\omega_{\rm pl}(q\hat{y})$, with (a) the wave vector q for different E_f values and (b) the Fermi energy for different q. The horizontal straight (orange) line denotes the $\omega_{\rm pl}(q\hat{x})/\omega_{\rm pl}(q\hat{y}) = \sqrt{m_y/m_x}$ line which is completely independent of the doping, based on plasmon dispersion calculated from the anisotropic parabolic dispersion in Eq. (9). The dashed horizontal line (violet) denotes Eq. (A10), which arises from the massive semi-Dirac plasmon dispersion, and it depends on the Fermi energy.

V. SUMMARY AND CONCLUSIONS

In this article we present a thorough study of the anisotropic EELS spectrum of monolayer phosphorene using the TDDFT framework. We find that the anisotropy of the underlying phosphorene crystal leads to the anisotropy in the band structure and, consequently, in the EELS spectrum as well—similarly to the case of bulk black phosphorus. For finite doping in the system, the lowest energy peak in the EELS corresponds to the intraband plasmon mode (charge density excitations) in the sub-electron-volt range. At slightly higher energy than the band gap, there is a highly dispersive low-energy exciton mode, which is almost independent of the doping and it is absent for the momentum transfer along the Γ-Y direction. At even higher energies and completely independent of the doping, there are various plasmon modes arising from the interband transitions with a very distinct peak appearing at ≈5 eV for monolayer phosphorene (as per GLLB calculations). With an increasing number of phosphorene layers (or thickness) this mode is likely to shift to higher energies, eventually merging into a 20-eV peak observed in the bulk black phosphorus. We explore the low-energy anisotropic intraband plasmons in detail and compare their behavior to analytical expression of the corresponding plasmon dispersion arising from the effective low-energy dispersion using RPA. The anisotropic intraband plasmon modes are found to be highly dispersive in nature, with the large-wavelength limit following the $\omega_{\rm pl} \propto \sqrt{q}$ behavior in all directions, which is a universal characteristic of plasmons in two dimensions. With increasing doping, the long-wavelength plasmon dispersion is found to scale with the Fermi energy as $\omega_{\rm pl} \propto \sqrt{E_f - E_c}$. The anisotropy of the long-wavelength plasmon dispersion is found to be inversely proportional to the ratio of square root of the effective masses: $\omega_{\rm pl}(q\hat{y})/\omega_{\rm pl}(q\hat{x}) = \sqrt{m_x/m_y}$.

ACKNOWLEDGMENTS

We acknowledge funding from the Department of Science and Technology (DST), Government of India, as follows: (i) DST INSPIRE Faculty Award, (ii) the Science and Engineering Research Board (SERB) Fast Track Scheme for Young Scientists, (iii) Ramanujan Fellowship, and (iv) DST Nanomission project. We also thank Computer Center Indian Institute of Technology (CC IITK), Kanpur for providing the High-Performance Computing (HPC) facility.

APPENDIX: LOW-ENERGY PLASMON DISPERSION OF PHOSPHORENE

Here we calculate the low-energy plasmon dispersion for a massive semi-Dirac system in two dimensions, described by Eq. (6). The polarization (density-density response) function is given by

$$\Pi(\vec{q},\omega) = \frac{g}{(2\pi)^d}\int d^dk \sum_{ss'=\pm} f^{ss'}(\mathbf{k},\mathbf{q})n_{\rm F}(E_{k,s}) \times\left(\frac{1}{\hbar\omega^+ + E_{\mathbf{k},s} - E_{\mathbf{k}',s'}} - \frac{1}{\hbar\omega^+ - E_{\mathbf{k},s} + E_{\mathbf{k}',s'}}\right), \tag{A1}$$

where $\omega^+ = \omega + i\eta$, $E_{k,s} = s\sqrt{v_f^2k_x^2 + (uk_y^2+\Delta)^2}$, $\mathbf{k}' = \mathbf{k} + \mathbf{q}$, $f^{ss'}(\mathbf{k},\mathbf{q})$ is the overlap function of spinors, and $n_F(E_{k,s})$ is the Fermi function. Expanding the polarization function defined in Eq. (A1), to q_x^2 and q_y^2 at zero temperature, leads to

$$\Pi(\mathbf{q}\to 0,\omega) = \frac{g}{4\pi^2}\int_{-\alpha}^{\alpha} dk_y \int_{-\beta}^{\beta} dk_x \times\left[I_1(k_x,k_y)\frac{v_f^2q_x^2}{\hbar^2\omega^2} + I_2(k_x,k_y)\frac{uq_y^2}{\hbar^2\omega^2}\right], \tag{A2}$$

where $\alpha = \sqrt{(E_f - \Delta)/u}$, $\beta = v_f^{-1}\sqrt{E_f^2 - (\Delta + uk_y^2)^2}$, and $I_{1,2}(k_x,k_y)$ are complex functions defined as follows:

$$I_1 = \frac{\left(\Delta + uk_y^2\right)^2}{\left[\left(\Delta + uk_y^2\right)^2 + k_x^2v_f^2\right]^{3/2}}, \tag{A3}$$

$$I_2 = \frac{2\left[\left(\Delta + uk_y^2\right)^3 + v_f^2k_x^2\left(\Delta + 3uk_y^2\right)\right]}{\left[\left(\Delta + uk_y^2\right)^2 + k_x^2v_f^2\right]^{3/2}}. \tag{A4}$$

Performing the integral in Eq. (A2), we obtain

$$\Pi(\mathbf{q}\to 0,\omega) = \frac{g}{4\pi^2\hbar^2\omega^2}\left\{v_f^2q_x^2{\rm Re}\zeta_1(E_f) + uq_y^2 \times[{\rm Re}\zeta_2(E_f) + {\rm Re}\zeta_3(E_f)]\right\}, \tag{A5}$$

where we have defined

$$\zeta_1(E_f) = -\frac{8i}{3v_fE_f}\sqrt{\frac{E_f-\Delta}{u}}[\Delta G_0(\nu) + E_fG_1(\nu)],$$

$$\zeta_2(E_f) = -\frac{32i}{15v_fE_f}\sqrt{\frac{E_f-\Delta}{u}}\left[\left(\Delta^2 + 3E_f^2\right)G_0(\nu), + (\Delta - 3E_f)E_fG_1(\nu)\right]$$

$$\zeta_3(E_f) = \frac{16iE_f}{v_f}\sqrt{\frac{E_f-\Delta}{u}}[G_0(\nu) - G_1(\nu)]. \tag{A6}$$

Equation (A6) in turn uses the following notation:

$$\nu = \sqrt{\frac{E_f-\Delta}{E_f+\Delta}}, \quad \phi = i{\rm arcsinh}(\nu),$$

$$G_0(\nu) = E\left[\phi, -\frac{1}{\nu^2}\right], \quad G_1(\nu) = F\left[\phi, -\frac{1}{\nu^2}\right], \tag{A7}$$

where $E[\phi, -\frac{1}{\nu^2}]$ and $F[\phi, -\frac{1}{\nu^2}]$ are incomplete elliptic integrals of the first and second kind, respectively.

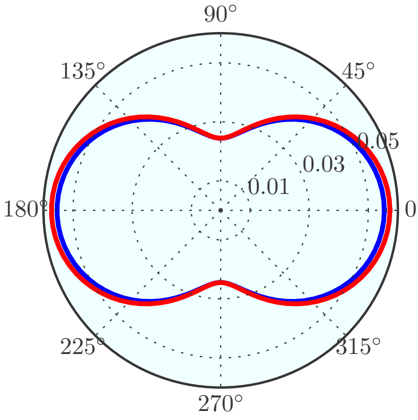

FIG. 8. Polar plot of the long wavelength plasmon dispersion [in units of $\sqrt{2e^2/(\hbar^2\epsilon)}$] of monolayer phosphorene. The red line is based on Eq. (9), and the red line is based on Eq. (A9). The radial and the azimuthal coordinates are the plasmon frequency, and the direction of the wave vector, where 0° (180°) and 90° (270°) indicate armchair (Γ-X) and the zigzag (Γ-Y) direction, respectively. The momentum is set to be $q = 0.02\,\text{Å}^{-1}$ and $E_f = 0.07$ eV.

Within RPA, the plasmons modes are given by the zeros of the longitudinal dielectric functions,

$$\varepsilon(q,\omega) = 1 - v_q \Pi(q,\omega) = 0, \tag{A8}$$

where v_q is the Fourier transform of the Coulomb potential. Substituting Eq. (A5) into Eq. (A8) immediately yields the long-wavelength plasmon dispersion to be

$$\omega_{\rm pl} = \beta_0 \sqrt{q}\big\{v_f^2 \cos^2\theta_q {\rm Re}\zeta_1(E_f) + u \sin^2\theta_q \times [{\rm Re}\zeta_2(E_f) + {\rm Re}\zeta_3(E_f)]\big\}^{1/2}, \tag{A9}$$

where we have used the two-dimensional form of $V_q = 2\pi e^2/(\epsilon q)$ and defined $\beta_0^2 = g e^2/(2\pi\hbar^2\epsilon)$. Figure 8 shows the angular dependence of the long-wavelength plasmon frequency, specified by Eq. (A9), and it matches reasonably well with the long-wavelength expression given in Eq. (9).

The ratio of the anisotropic plasmon dispersion in x and y direction for same value of the wave vector (in the long-wavelength regime) is given by

$$\frac{\omega_{\rm pl}(q\hat{x})}{\omega_{\rm pl}(q\hat{y})} = \sqrt{\frac{v_f^2 {\rm Re}\zeta_1(E_f)}{u[{\rm Re}\zeta_2(E_f) + {\rm Re}\zeta_3(E_f)]}}. \tag{A10}$$

[1] A. K. Geim and K. S. Novoselov, The rise of graphene, Nat. Mater. **6**, 183 (2007).

[2] F. Schwierz, Graphene transistors, Nat. Nanotechnol. **5**, 487 (2010).

[3] B. Radisavljevic, A. Radenovic, J. Brivio, V. Giacometti, and A. Kis, Single-layer mos2 transistors, Nat. Nanotechnol. **6**, 147 (2011).

[4] Z. S. Butler *et al.*, Progress, challenges, and opportunities in two-dimensional materials beyond graphene, ACS Nano **7**, 2898 (2013).

[5] B. Dubertret, T. Heine, and M. Terrones, The rise of two-dimensional materials, Acc. Chem. Res. **48**, 1 (2015).

[6] H. Liu, A. T. Neal, Z. Zhu, Z. Luo, X. Xu, D. Tománek, and P. D. Ye, Phosphorene: An unexplored 2d semiconductor with a high hole mobility, ACS Nano **8**, 4033 (2014).

[7] L. Li, Y. Yu, G. J. Ye, Q. Ge, X. Ou, H. Wu, D. Feng, X. H. Chen, and Y. Zhang, Black phosphorus field-effect transistors, Nat. Nanotechnol. **9**, 372 (2014).

[8] Z. Zhu and D. Tománek, Semiconducting Layered Blue Phosphorus: A computational Study, Phys. Rev. Lett. **112**, 176802 (2014).

[9] B. Ghosh, S. Nahas, S. Bhowmick, and A. Agarwal, Electric field induced gap modification in ultrathin blue phosphorus, Phys. Rev. B **91**, 115433 (2015).

[10] K. S. Novoselov, A. Mishchenko, A. Carvalho, and A. H. Castro Neto, 2d materials and van der waals heterostructures, Science **353**, aac9439 (2016).

[11] S. Nahas, B. Ghosh, S. Bhowmick, and A. Agarwal, First-principles cluster expansion study of functionalization of black phosphorene via fluorination and oxidation, Phys. Rev. B **93**, 165413 (2016).

[12] S. Mardanya, V. K. Thakur, S. Bhowmick, and A. Agarwal, Four allotropes of semiconducting layered arsenic that switch into a topological insulator via an electric field: Computational study, Phys. Rev. B **94**, 035423 (2016).

[13] X. Ling, H. Wang, S. Huang, F. Xia, and M. S. Dresselhaus, The renaissance of black phosphorus, Proc. Natl. Acad. Sci. USA **112**, 4523 (2015).

[14] J. Qiao, X. Kong, Z-X. Hu, F. Yang, and W. Ji, High-mobility transport anisotropy and linear dichroism in few-layer black phosphorus, Nat. Commun. **5**, 4475 (2014).

[15] A. S. Rodin, A. Carvalho, and A. H. Castro Neto, Strain-Induced Gap Modification in Black Phosphorus, Phys. Rev. Lett. **112**, 176801 (2014).

[16] A. N. Rudenko and M. I. Katsnelson, Quasiparticle band structure and tight-binding model for single- and bilayer black phosphorus, Phys. Rev. B **89**, 201408 (2014).

[17] M. Ezawa, Topological origin of quasi-flat edge band in phosphorene, New J. Phys. **16**, 115004 (2014).

[18] T-H. Liu and C-C. Chang, Anisotropic thermal transport in phosphorene: effects of crystal orientation, Nanoscale **7**, 10648 (2015).

[19] V. Tran, R. Soklaski, Y. Liang, and L. Yang, Layer-controlled band gap and anisotropic excitons in few-layer black phosphorus, Phys. Rev. B **89**, 235319 (2014).

[20] T. Low, R. Roldán, H. Wang, F. Xia, P. Avouris, L. Martín Moreno, and F. Guinea, Plasmons and Screening in Monolayer and Multilayer Black Phosphorus, Phys. Rev. Lett. **113**, 106802 (2014).

[21] A. S. Rodin and A. H. Castro Neto, Collective modes in anisotropic double-layer systems, Phys. Rev. B **91**, 075422 (2015).

[22] R. F. Egerton, Electron energy-loss spectroscopy in the tem, Rep. Prog. Phys. **72**, 016502 (2009).

[23] T. Eberlein, U. Bangert, R. R. Nair, R. Jones, M. Gass, A. L. Bleloch, K. S. Novoselov, A. Geim, and P. R. Briddon, Plasmon spectroscopy of free-standing graphene films, Phys. Rev. B **77**, 233406 (2008).

[24] S. Y. Shin, N. D. Kim, J. G. Kim, K. S. Kim, D. Y. Noh, K. S. Kim, and J. W. Chung, Control of the plasmon in a single layer graphene by charge doping, Appl. Phys. Lett. **99**, 082110 (2011).

[25] M. K. Kinyanjui, C. Kramberger, T. Pichler, J. C. Meyer, P. Wachsmuth, G. Benner, and U. Kaiser, Direct probe of linearly dispersing 2d interband plasmons in a free-standing graphene monolayer, Europhys. Lett. **97**, 57005 (2012).

[26] C. Tegenkamp, H. Pfnür, T. Langer, J. Baringhaus, and H. W. Schumacher, Plasmon electron–hole resonance in epitaxial graphene, J. Phys.: Condens. Matter **23**, 012001 (2011).

[27] T. Langer, J. Baringhaus, H. Pfnür, H. W. Schumacher, and C. Tegenkamp, Plasmon damping below the landau regime: the role of defects in epitaxial graphene, New J. Phys. **12**, 033017 (2010).

[28] S. C. Liou, C.-S. Shie, C. H. Chen, R. Breitwieser, W. W. Pai, G. Y. Guo, and M.-W. Chu, π- plasmon dispersion in free-standing graphene by momentum-resolved electron energy-loss spectroscopy, Phys. Rev. B **91**, 045418 (2015).

[29] C. Kramberger *et al.*, Linear Plasmon Dispersion in Single-Wall Carbon Nanotubes and the Collective Excitation Spectrum of Graphene, Phys. Rev. Lett. **100**, 196803 (2008).
[30] J. Yan, K. S. Thygesen, and K. W. Jacobsen, Nonlocal Screening of Plasmons in Graphene by Semiconducting and Metallic Substrates: First-Principles Calculations, Phys. Rev. Lett. **106**, 146803 (2011).
[31] J. N. Coleman *et al.*, Two-dimensional nanosheets produced by liquid exfoliation of layered materials, Science **331**, 568 (2011).
[32] P. Johari and V. B. Shenoy, Tunable dielectric properties of transition metal dichalcogenides, ACS Nano **5**, 5903 (2011).
[33] R. Schuster, J. Trinckauf, C. Habenicht, M. Knupfer, and B. Büchner, Anisotropic Particle-Hole Excitations in Black Phosphorus, Phys. Rev. Lett. **115**, 026404 (2015).
[34] B. Wunsch, T. Stauber, F. Sols, and F. Guinea, Dynamical polarization of graphene at finite doping, New J. Phys. **8**, 318 (2006).
[35] R. Sachdeva, A. Thakur, G. Vignale, and A. Agarwal, Plasmon modes of a massive dirac plasma, and their superlattices, Phys. Rev. B **91**, 205426 (2015).
[36] A. Hill, S. A. Mikhailov, and K. Ziegler, Dielectric function and plasmons in graphene, Europhys. Lett. **87**, 27005 (2009).
[37] K.-T. Lam and J. Guo, Plasmonics in strained monolayer black phosphorus, J. Appl. Phys. **117**, 113105 (2015).
[38] F. Jin, R. Roldán, M. I. Katsnelson, and S. Yuan, Screening and plasmons in pure and disordered single- and bilayer black phosphorus, Phys. Rev. B **92**, 115440 (2015).
[39] E. H. Hwang and S. D. Sarma, Dielectric function, screening, and plasmons in two-dimensional graphene, Phys. Rev. B **75**, 205418 (2007).
[40] A. Agarwal and G. Vignale, Plasmons in spin-polarized graphene: A way to measure spin polarization, Phys. Rev. B **91**, 245407 (2015).
[41] K. Andersen and K. S. Thygesen, Plasmons in metallic monolayer and bilayer transition metal dichalcogenides, Phys. Rev. B **88**, 155128 (2013).
[42] C. V. Gomez, M. Pisarra, M. Gravina, J. M. Pitarke, and A. Sindona, Plasmon Modes of Graphene Nanoribbons with Periodic Planar Arrangements, Phys. Rev. Lett. **117**, 116801 (2016).
[43] V. Despoja, D. Novko, K. Dekanić, M. Šunjić, and L. Marušić, Two-dimensional and π plasmon spectra in pristine and doped graphene, Phys. Rev. B **87**, 075447 (2013).
[44] S. Kaltenborn and H. C. Schneider, Plasmon dispersions in simple metals and heusler compounds, Phys. Rev. B **88**, 045124 (2013).
[45] K. Andersen, K. W. Jacobsen, and K. S. Thygesen, Plasmons on the edge of mos$_2$ nanostructures, Phys. Rev. B **90**, 161410 (2014).
[46] P. E. Trevisanutto, C. Giorgetti, L. Reining, M. Ladisa, and V. Olevano, *Ab Initio* GW Many-Body Effects in Graphene, Phys. Rev. Lett. **101**, 226405 (2008).
[47] S. L. Adler, Quantum theory of the dielectric constant in real solids, Phys. Rev. **126**, 413 (1962).
[48] N. Wiser, Dielectric constant with local field effects included, Phys. Rev. **129**, 62 (1963).
[49] C. A. Rozzi, D. Varsano, A. Marini, E. K. U. Gross, and A. Rubio, Exact coulomb cutoff technique for supercell calculations, Phys. Rev. B **73**, 205119 (2006).
[50] J. J. Mortensen, L. B. Hansen, and K. W. Jacobsen, Real-space grid implementation of the projector augmented wave method, Phys. Rev. B **71**, 035109 (2005).
[51] J. Enkovaara *et al.*, Electronic structure calculations with gpaw: A real-space implementation of the projector augmented-wave method, J. Phys.: Condens. Matter **22**, 253202 (2010).
[52] S. R. Bahn and K. W. Jacobsen, An object-oriented scripting interface to a legacy electronic structure code, Comput. Sci. Eng. **4**, 56 (2002).
[53] O. Gritsenko, R. V. Leeuwen, E. V. Lenthe, and E. J. Baerends, Self-consistent approximation to the kohn-sham exchange potential, Phys. Rev. A **51**, 1944 (1995).
[54] G. Giuliani and G. Vignale, *Quantum Theory of the Electron Liquid*, Masters Series in Physics and Astronomy (Cambridge University Press, Cambridge, 2005).
[55] P. Kumar, B. S. Bhadoria, S. Kumar, S. Bhowmick, Y. S. Chauhan, and A. Agarwal, Thickness and electric-field-dependent polarizability and dielectric constant in phosphorene, Phys. Rev. B **93**, 195428 (2016).
[56] B. Ghosh, B. Singh, R. Prasad, and A. Agarwal, Electric-field tunable dirac semimetal state in phosphorene thin films, Phys. Rev. B **94**, 205426 (2016).
[57] S. D. Sarkar, A. Agarwal, and K. Sengupta, Anisotropic transport of normal metal-barrier-normal metal junctions in monolayer phosphorene, J. Phys.: Condens. Matter **29**, 285601 (2017).
[58] R. J. Wu, M. Topsakal, T. Low, M. C. Robbins, N. Haratipour, J. S. Jeong, R. M. Wentzcovitch, S. J. Koester, and K. A. Mkhoyan, Atomic and electronic structure of exfoliated black phosphorus, J. Vac. Sci. Technol. A **33**, 060604 (2015).
[59] L. Li *et al.*, Direct observation of the layer-dependent electronic structure in phosphorene, Nat. Nano **12**, 21 (2016).
[60] A. N. Rudenko, S. Yuan, and M. I. Katsnelson, Toward a realistic description of multilayer black phosphorus: From GW approximation to large-scale tight-binding simulations, Phys. Rev. B **92**, 085419 (2015).
[61] J. M. Pereira and M. I. Katsnelson, Landau levels of single-layer and bilayer phosphorene, Phys. Rev. B **92**, 075437 (2015).
[62] E. Motohiko, Highly anisotropic physics in phosphorene, J. Phys.: Conf. Ser. **603**, 012006 (2015).
[63] X. Wang, A. M. Jones, K. L. Seyler, V. Tran, Y. Jia, H. Zhao, H. Wang, L. Yang, X. Xu, and F. Xia, Highly anisotropic and robust excitons in monolayer black phosphorus, Nat Nano **10**, 517 (2015).